Competing boundary effects on bubble collapse jets near a semi-submerged cylinder*

Haojie Bian (边豪杰),[1] Hongchen Su (苏泓臣),[1] Junwei Shen (沈钧炜),[1] Jiaxin Yu (于佳鑫),[1] Peng Luo (罗鹏),[1] and Yuning Zhang (张宇宁) [1,†]

[1]*Key Laboratory of Power Station Energy Transfer Conversion and System (Ministry of Education), School of Energy Power and Mechanical Engineering, North China Electric Power University, Beijing 102206, China*

The present paper conducts a systematic analysis of the bubble dynamic behaviors in the vicinity of a semi-submerged cylinder. A theoretical model for the bubble oscillation near the semi-submerged cylinder is established. The influence of the semi-submerged cylinder on the liquid velocity, jet, and impulse characteristics is qualitatively and quantitatively investigated. Furthermore, the jet attraction region and the impulse-dominated region are delineated. The main conclusions are outlined below: (1) The jet direction can be effectively predicted by the direction of the maximum liquid velocity on the bubble interface. Among the factors affecting the liquid velocity, the free surface dominates the liquid velocity contribution over approximately 70% of the parametric range, whereas the cylinder dictates the rest. (2) The bubble collapse jets are classified into the jet pointing towards the cylinder and the jet not pointing towards the cylinder. The impulse attraction region of the cylinder is confined to a relatively small area in its vicinity, correlating with the cylinder radius and spanning approximately 1.1 times its cross-sectional area. (3) The impulse contributed by the cylinder and the free surface are opposite in direction, and a region of minimum impulse intensity and highest impulse sensitivity is present directly below the cylinder.

Keywords: bubble dynamics, jet, Kelvin impulse, cylinder, free surface
PACS: 47.55.Bx, 47.55.Dz

1. Introduction

Cavitation is a complex process in which the liquid vaporizes and forms bubbles in a low-pressure environment, and these bubbles collapse in high-pressure regions. This phenomenon is widely observed in fields such as hydraulic machinery, ultrasonic research, and ocean engineering.[1-5] When a rigid wall is partially submerged in a liquid, a unique pressure gradient field is formed at the junction between the rigid wall and the free surface, leading to the generation, evolution, and collapse of the bubble. During this process, not only does it induce structural vibration, noise radiation, and material

* National Natural Science Foundation of China (Project Nos.: 52506045), Fundamental Research Funds for the Central Universities (2025JC011)
† Corresponding author. E-mail: yuning.zhang@foxmail.com

erosion, but it may also pose challenges to the stability and safety of the system.[6-10] In this scenario, the free surface under semi-submerged conditions significantly alters the bubble dynamics.[11-13] Furthermore, when the process occurs within confined spaces, it triggers more complex cavitation phenomena.[14-15] Therefore, the present paper conducts an in-depth investigation into the cavitation phenomena near a semi-submerged cylinder within confined spaces, covering aspects such as the jet generation mechanism, the impulse transfer law, and the centroid movement.

The physical scenarios of the cavitation research can be simply classified into three categories: rigid walls, free surfaces, and joint effects of both.[16-18] Regarding rigid walls, extensive foundational work has established the fundamental mechanisms. Early studies by Plesset et al.[19] and Lauterborn[20] laid the theoretical and experimental groundwork, revealing the formation of high-speed jets and localized high-pressure regions during collapse. Subsequent investigations further quantified the influence of boundary geometry, such as the erosion mechanisms identified by Brujan et al.[21] and the curvature effects reported by Tomita et al.[22]. Building upon these fundamental understandings, more recent studies have focused on complex configurations. Bhola et al.[23] examined the bubble behaviors under a shear flow adjacent to a rigid wall. They found that the flow induces bubble deformation and the subsequent generation of two re-entrant jets. Shen et al.[24] examined how the geometry of a rigid boundary affects the jet impact behaviors resulting from the bubble collapse. They found that a smaller wall curvature leads to a higher peak jet impact pressure. The impact area was observed to expand with increasing wall curvature. Wang et al.[25] investigated the dynamic behaviors of confined bubbles near a right-angled wall. They found that jet velocity is closely related to the wall distance—the smaller the distance, the higher jet velocity. Shen et al.[26] explored the influence of flat walls and cylinders on the bubble dynamics within confined spaces, demonstrating that the liquid velocity distribution can accurately describe the bubble interface's motion.

Regarding the free surfaces, researchers have delineated their critical role in governing bubble collapse behaviors, particularly in inducing high-speed jets, altering morphological evolution, and enhancing interfacial mixing. Boulton-Stone et al.[27]

investigated the bubble behaviors in the vicinity of a free surface, finding that the collapse process generates a high-speed jet and ejects small droplets. Zhang et al.[28] investigated the jet phenomenon resulting from the interaction between a cavitation vortex ring and the free surface, revealing the formation mechanism and critical conditions of a single high-speed jet. They found that when the bubble is trapped within a stable cavitation vortex ring and approaches the free surface, it generates a unidirectional high-speed jet with excellent directivity. Ma et al.[29] utilized the high-speed photography system to examine the bubble dynamic characteristics beneath the free surface within confined spaces. They observed that as the bubble to free surface distance decreases and the height of the confined spaces increases, the jet morphology transitions from an arc shape to an angular shape. Han et al.[30] revealed the fluid mixing mechanism induced by the bubble collapse. They found that when the bubble is generated in the oil phase, the high-speed jet produced during collapse penetrates the water-oil interface. The critical penetration conditions are strongly governed by the density ratio of the two fluids. Li et al.[31] explored the bubble dynamic behaviors within droplets suspended in heterogeneous fluids, finding that during the collapse of the bubble in an oil-in-water droplet, a high-speed micro-jet penetrates the droplet interface, enabling mass transport from the oil phase to the water phase. Conversely, when the bubble is located in a water-in-oil droplet, it is collapsed by the droplet surface, and the resulting bubble vortex ring migrates along the droplet, facilitating mass transport from the water phase to the oil phase.

When the rigid wall and the free surface coexist, the cavitation research must consider the combined influence of the rigid wall constraints and the free surface fluctuations on the bubbles. Recent work utilizing multi-physics coupled models has revealed the energy transfer mechanism among the rigid wall, bubble, and free surface. Liu et al.[11] systematically investigated the bubble dynamic characteristics under the combined boundary of a free surface and a flat plate with a circular hole. They found that when the bubble is generated near the center of the circular hole, opposite-jets form during bubble collapse. Kiyama et al.[32] proposed a theoretical model using image methods to predict the direction of the jets in the angular region. They found that when the bubble

is near a rigid wall, the micro-jet points perpendicularly toward the wall. Conversely, when the bubble is near a free surface, the micro-jet points away from the wall. Sun et al.[33] achieved control over the bubble collapse direction and jets by arranging free and rigid boundaries. As the geometric parameters vary, the bubbles exhibit three distinct modes: a micro-jet pointing towards the rigid boundary, an approximately spherical symmetric collapse, and an annular micro-jet.

Existing studies indicate that the rigid wall exerts a repulsive effect on the bubble, whereas the free surface attracts it. When the bubble collapse occurs near the confluence of these two boundaries, more complex dynamic behaviors emerge. However, research on the bubble dynamics under such conditions within confined spaces remains limited. Particularly, physical constraints force bubbles into a cylindrical morphology within confined spaces, leading to collapse patterns and jet characteristics that differ markedly from those of spherical bubbles in unconstrained fields. In engineering applications, such conditions characterized by dual boundary effects superimposed with geometric confinement are prevalent. For instance, the narrow flow passages between turbine runner blades and stay vanes, as well as the annular gaps between the spool and sleeve of hydraulic cylindrical valves, represent high-risk zones for cavitation erosion.[34,35] Therefore, elucidating the mechanisms governing bubble dynamics near a semi-submerged cylinder within confined spaces is essential, which holds theoretical value for revealing the underlying causes of cavitation damage in hydraulic machinery.

The present paper conducts a systematic analysis of the bubble behaviors in the vicinity of a semi-submerged cylinder by utilizing the high-speed photography and Kelvin impulse theory. The sections are arranged as follows: Section 2 presents the theoretical methods for the bubble dynamics near a semi-submerged cylinder within confined spaces. Section 3 introduces the high-speed photography experimental system. Section 4 analyzes the bubble collapse jets and morphological characteristics. Section 5 mainly investigates the bubble centroid movement and the impulse field. Section 6 synthesizes the conclusions of the present paper.

2. Theoretical model

This section introduces the boundary treatment method and derives the expression for the Kelvin impulse near a semi-submerged cylinder. When the bubble oscillates within confined spaces, the bubble interface's motion perpendicular to the glass plate is constrained, causing the bubble to exhibit a cylindrical shape. Since only the radial motion of the bubble is considered, it can be treated as a two-dimensional point source. The theoretical model is developed based on the theory of inviscid, irrotational, and incompressible potential flow. Within the potential flow framework, the free surface is treated using the image methods. The present paper selects the dimensionless time of 0.75 for analyzing the bubble dynamics, at which the bubble retains a well-defined cylindrical shape, ensuring the validity of the theoretical model. Laser-induced cavitation operates at high Reynolds number, where the boundary layer thickness is negligible compared to the bubble scale. The Reynolds number can be obtained as follows:

$$\mathrm{Re} = \frac{R_{\max}\rho U}{\mu}. \tag{1}$$

Here, the characteristic velocity $U = \sqrt{P_\infty / \rho} \approx 10$ m/s , water density $\rho = 1000$ kg/m^3 , and $\mu = 10^{-3}$ $Pa \cdot s$. Considering the $\mathrm{Re} \sim \mathrm{O}\left(10^5\right) \gg 1$, the viscosity is negligible.

For the specific configuration of a semi-submerged cylinder, the present paper combines the image method and the circle theorem to solve the free surface and cylinder boundary conditions, respectively. By integrating these mathematical methods, a composite flow field model is developed that simultaneously satisfies the kinematic conditions of both the rigid wall and the free surface. In addition, based on the Kelvin impulse theory, the force and impulse exerted on the bubble near the semi-submerged cylinder are derived, and the bubble migration motion is also considered.

Figure 1 illustrates the boundary treatment for the semi-submerged cylinder. In the figure, the gray circle represents the cylinder, while the white circles with solid and dashed lines denote the bubble and the image bubble, respectively. The complex potential of the two-dimensional point source (f_0) is given as follows:[26]

$$f_0(z) = \frac{m}{2\pi}\ln\left(z - z_0\right), \tag{2}$$

where

$$m = 2\pi hR\dot{R}, \tag{3}$$

$$z_0 = x_0 + iy_0. \tag{4}$$

Here, m denotes the strength of the two-dimensional point source, z_0 represents the complex coordinate of the point source, h denotes the height of the cylindrical bubble. Furthermore, R and $\dot{R}$ represent the bubble radius and the time derivative of the radius, respectively. When the bubble oscillates near the free surface, the surface's influence can be treated as an image bubble, and the expression for its complex potential (f_1) is given as follows:[26]

$$f_1 = -\frac{m}{2\pi}\ln(z - z_1). \tag{5}$$

Here, z_1 represents the complex coordinate of the image bubble, $z_1 = \overline{z}_0$.

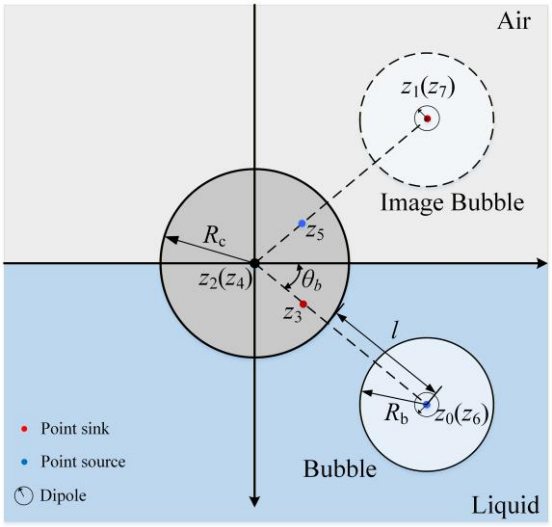


FIG. 1. Boundary treatment of the semi-submerged cylinder.

When the bubble oscillates near the cylinder, according to the circle theorem, the influence of the cylinder can be treated as the superposition of a point source and a point sink. Applying the circle theorem to the bubble, the complex potential generated by the cylinder is given as follows:

$$f_2 = \frac{m}{2\pi}\ln(z - z_2), \tag{6}$$

$$f_3 = -\frac{m}{2\pi}\ln(z - z_3), \tag{7}$$

where

$$z_3 = z_2 - \frac{R_c^2}{\overline{z_2 - z_0}}. \tag{8}$$

Here, R_c represents the radius of the cylinder.

Similarly, applying the circle theorem to the image bubble, the complex potential generated by the cylinder is given as follows:

$$f_4 = -\frac{m}{2\pi}\ln(z - z_4), \tag{9}$$

$$f_5 = \frac{m}{2\pi}\ln(z - z_5), \tag{10}$$

where

$$z_5 = z_4 - \frac{R_c^2}{\overline{z_4 - z_1}}. \tag{11}$$

Considering the movement of the bubble during oscillation, dipoles are introduced. The dipoles of the bubble and the image bubble are given as follows:

$$f_6 = \frac{D}{2\pi}\left(\frac{1}{z - z_6}\right), \tag{12}$$

$$f_7 = \frac{D}{2\pi}\left(\frac{1}{z - z_7}\right), \tag{13}$$

where

$$D = \pi h R^2 (v_x + i v_y). \tag{14}$$

Here, D represents the dipole strength, and v_x and v_y are the components of the bubble's velocity in the x and y directions, respectively, which are determined by experimental measurements. Therefore, by integrating the image method and the circle theorem to address the boundary conditions, the complex potential of the liquid near the semi-submerged cylinder is given as follows:

$$F(z) = \frac{m}{2\pi}\ln\frac{(z - z_0)(z - z_2)(z - z_5)}{(z - z_1)(z - z_3)(z - z_4)} + \frac{D}{2\pi}\left(\frac{1}{z - z_6} + \frac{1}{z - z_7}\right). \tag{15}$$

The expression for the velocity potential of the liquid is given as follows:

$$\boldsymbol{u} = \frac{\delta\{\mathrm{Re}[F(z)]\}}{\delta x}\cdot\boldsymbol{e}_x + \frac{\delta\{\mathrm{Re}[F(z)]\}}{\delta y}\cdot\boldsymbol{e}_y. \tag{16}$$

Therefore, the formula for impulse is expressed as follows:[34]

$$I = -4\pi h\rho\int_0^T \left\{\nabla \mathrm{Re}\left[F(z) - f_0(z)\right]\right\}_{z_0} R\dot{R}dt. \tag{17}$$

Here, ρ represents the liquid density, and T represents the period of the bubble oscillation.

Hence, numerical results of the Kelvin impulse can be acquired. To complete the modeling framework and further deduce its analytical expression, the radial dynamic equation of the cylindrical bubble is then incorporated. The equation employed in this study is expressed as follows:[35]

$$\left(\dot{R}^2 + R\ddot{R}\right)\ln\frac{r_{\mathrm{m}}}{R} - \frac{1}{2}\dot{R}^2 = \frac{p_R - p_\infty}{\rho}, \tag{18}$$

where

$$p_R = \left(p_\infty + \frac{\sigma}{R_0}\right)\left(\frac{R_0}{R}\right)^{2\kappa} - \frac{\sigma}{R}. \tag{19}$$

Here, $\ddot{R}$ represents the second derivative of R with respect to time, r_{m} denotes the prescribed maximum radial distance within the flow field under investigation, p_R represents the liquid pressure on the bubble interface, p_∞ denotes the ambient pressure, $p_\infty = 10^5$ Pa, κ denotes the polytropic index, $\kappa = 1.4$, R_0 represents the bubble equilibrium radius σ represents the surface tension coefficient, $\sigma = 0.0725$ N/m.

To simplify the ensuing analysis, a set of dimensionless parameters are introduced below:

$$X^* = \frac{x}{R_{\max}}, \tag{20}$$

$$Y^* = \frac{y}{R_{\max}}, \tag{21}$$

$$l^* = \frac{l}{R_{\max}}, \tag{22}$$

$$R_{\mathrm{c}}^* = \frac{R_{\mathrm{c}}}{R_{\max}}, \tag{23}$$

$$t^* = \frac{t}{T}. \tag{24}$$

In the above equations, x and y denote the spatial coordinates, $R_{\max}$ is the

maximum radius of the bubble, l is the bubble centroid to the cylinder surface distance and t is the time.

In addition, the values used to solve the above formula are given as follows: $h = 1.5$ mm; $R_{\max} = 1.8$ mm. Based on the aforementioned equations, MATLAB is used to theoretically calculate the Kelvin impulse and the liquid velocity. The instant $t^* = 0.75$ is selected for analyzing the velocity field, at which the bubble retains a well-defined cylindrical shape.

3. Experimental setup

This section introduces the experimental system and the procedure. The errors generated during the experiment are also analyzed. The models used in the experiment and their arrangement are shown in Figure 2. During the experiment, two glass plates are arranged in parallel to form a two-dimensional region. A glass cylinder is placed between the plates, and this assembly is submerged in a water tank filled with deionized water. The laser emitted from a laser generator is focused between the glass plates after passing through a beam expander and a focusing lens, creating a cylindrical bubble. A signal delay generator is used to coordinate the laser generation and the camera's shooting in order to capture the complete bubble oscillation process. A light source is placed directly behind the water tank to provide backlighting for the camera.

Subsequently, an analysis of the experimental errors is presented. For the quantitative analysis, the data for calculating distances and angles are obtained from the high-speed photographic images. The horizontal and vertical errors correspond to the length of one pixel in the image, which is 0.0486 mm. Therefore, the distance error (Δs_{e}) is given as follows:

$$\Delta s_{\mathrm{e}} = \pm\sqrt{\Delta x^2 + \Delta y^2} = \pm 0.0687 \text{ mm}. \tag{25}$$

Here, Δx and Δy represent the horizontal and vertical errors, respectively. When calculating the jet angle, the angle error ($\Delta\theta_{\mathrm{e}}$) is given as follows:

$$\Delta\theta_{\mathrm{e}} = \arctan\frac{\Delta s_{\mathrm{e}}}{2R_{\max}} = \pm 1.093^\circ. \tag{26}$$

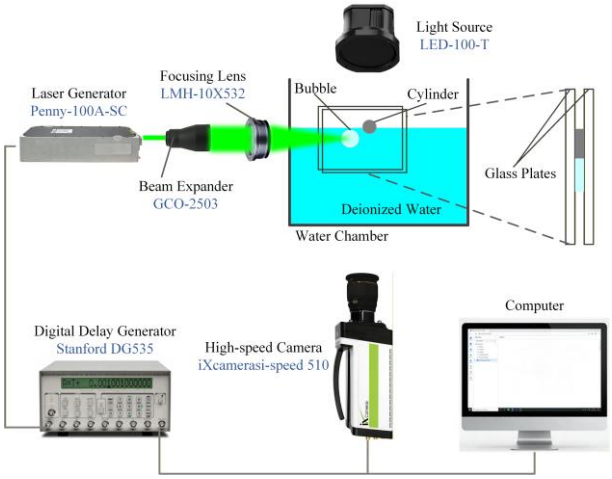


FIG. 2. Schematic diagram of the experimental platform.

Table 1. Summary table of experimental equipment specifications.

Equipment	Brand	Parameters
Laser Generator	Ziyu (Penny-100A-SC)	Pulse energy: 50 mJ Laser wavelength: 532 nm
High-speed Camera	iXcameras (i-speed 510)	Shooting frame rate: 50,000 fps Resolution: 256×256 pixels
Digital Delay Generator	Stanford (DG535)	Resolution: 5 pixels
Light Source	Jinqiao (LED-100-T)	Maximum power: 100W
Beam Expander	Daheng Optics (GCO-2503)	Beam expansion ratio: 5x
Focusing Lens	Thorlabs (LMH-10X532)	Focal length: 50 mm
Water Chamber	Glass material	Water temperature:20 ℃

4. Analysis of the bubble collapse jets and morphological characteristics

4.1 Symmetric position

In this section, the bubble collapse jets are analyzed qualitatively and quantitatively. The influences of the bubble-cylinder distance, the bubble-free surface distance, and the cylinder radius on the jet morphologies are presented.

Figure 3 illustrates the typical morphological evolution of the bubble collapse process. The yellow dashed line in the figure indicates the bubble centroid position when the bubble is at its maximum radius. The dark regions on the cylindrical surface arise from

the intense liquid microjet generated during the bubble collapse near the free surface. Constrained by the geometric boundary of the cylinder, this high-speed flow is forced to bifurcate, thereby forming two distinct dark patches on the surface. The variation in both direction and distance of the bubble centroid migration arises from the opposing effects of the rigid cylindrical wall and the free surface. While the rigid wall exerts an attractive force on the bubble, the free surface imposes a repulsive force. In subfigure (a), the cylinder radius is relatively small. At this stage, the influence of the cylinder is less significant than that of the free surface. Consequently, the bubble gradually moves away from the cylinder, and the jet is oriented vertically downward. In subfigure (b), as the cylinder radius increases, the influences of the cylinder and the free surface on the bubble become approximately equal. The bubble shows almost no movement during the collapse phase, and two weak symmetrical jets appear at the upper left and right sides of the bubble. In subfigure (c), with a further increase in the cylinder radius, the cylinder's influence becomes dominant over that of the free surface. The bubble migrates toward the cylinder during collapse, and two weak jets emerge on the left and right sides of the lower part of the bubble. Spherical and cylindrical bubbles exhibit markedly distinct collapse characteristics. High-speed imaging reveals that spherical bubbles resemble solid spheres, whereas cylindrical bubbles appear as annular bubbles. When approaching a particle, the jet behavior of the spherical bubble manifests as bubble elongation.[38] In contrast, the jet behavior of the cylindrical bubble near a semi-submerged cylinder presents as bubble truncation. Moreover, the jet of the cylindrical bubble emerges during the first collapse cycle, whereas the jet of the spherical bubble occurs in the second collapse cycle. In addition, for the present model, when the free surface in the semi-submerged cylinder model is replaced by a rigid wall, the configuration becomes a wall with a semi-cylindrical protrusion. The bubble exhibits distinct characteristics compared to that near a semi-submerged cylinder.[39] Owing to the wall's attractive effect, the bubble centroid consistently migrates toward the wall across different cylinder radii, and the jet direction remains oriented toward the semi-cylindrical protrusion.

Figure 4 displays the theoretical results for the liquid velocity distribution near the semi-

submerged cylinder, where different colors represent the velocity magnitude, and the length and orientation of the arrows correspond to the magnitude and direction of the local liquid velocity. In the figure, when the cylinder radius is small (subfigure (a)), the semi-submerged cylinder exerts a relatively weak macroscopic obstructive effect on the surrounding flow field. The symmetrical high-velocity regions exist on both sides of the cylinder and on the left and right sides above the bubble. A low-velocity region is present on the lower surface of the cylinder. As the cylinder radius increases, it acts as an imposing physical boundary, inducing a pronounced deflection of the streamlines. The high-velocity regions on both sides of the cylinder gradually shrink, and the high-velocity region around the bubble shifts downward. Relative to the spherical bubble, the high-speed liquid region around the cylindrical bubble has a markedly lower velocity—only half that surrounding its spherical counterparts.[38] Changes in the velocity field directly cause the variations in the morphology of the bubble collapse. The dashed lines in Figure 4 trace the experimentally observed bubble contour evolution during collapse. The evolution trend of the bubble contour varies significantly with the liquid velocity distribution: the higher the liquid velocity on the bubble interface, the faster the contour contracts.

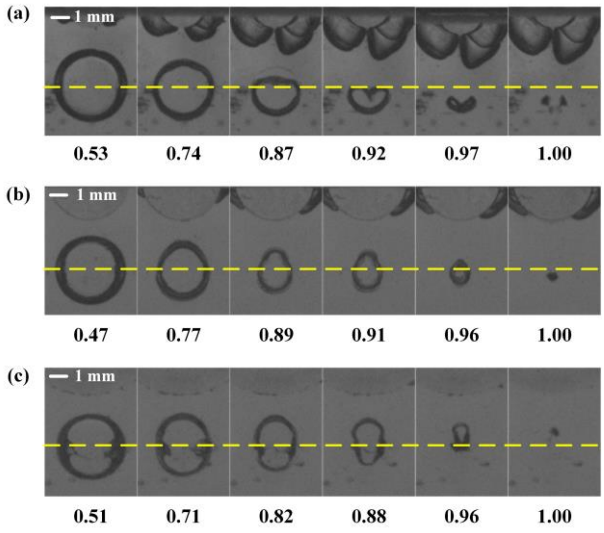


FIG. 3. High-speed photographs of the bubble oscillation at $l^* = 2.5$. (a) $R_c^* = 0.56$. (b) $R_c^* = 1.11$. (c) $R_c^* = 2.22$.

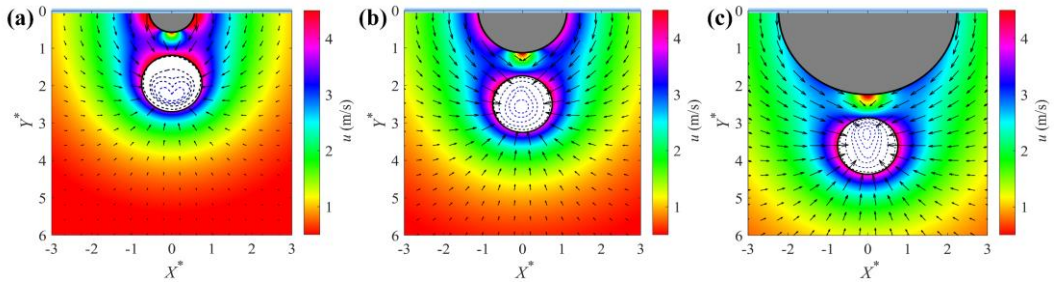


FIG.4. The liquid velocity distribution and the bubble contour evolution during collapse with different cylinder radii (R_c^*) at $l^* = 2.5$. (a) $R_c^* = 0.56$. (b) $R_c^* = 1.11$. (c) $R_c^* = 2.22$. The background color map and arrows denote the numerically computed velocity field, while the dashed lines indicate the experimentally observed bubble contours during collapse.

Figure 5 illustrates the velocity distribution on the bubble interface. The radar chart in the figure displays the positions and magnitudes of the maximum velocity (u_{max}) and the minimum velocity (u_{min}) of the bubble interface's motion. It can be observed that the velocity distribution on the bubble interface is symmetrical, exhibiting a trend of first increasing and then decreasing from the top vertex to the bottom vertex. As the cylinder radius increases, the position of u_{max} gradually shifts downward, and the position of u_{min} remains at the top or bottom vertex. The variation between u_{max} and u_{min} is related to the bubble interface's motion in the experiment. The presence of the u_{max} induces indentation of the bubble interface at that location.

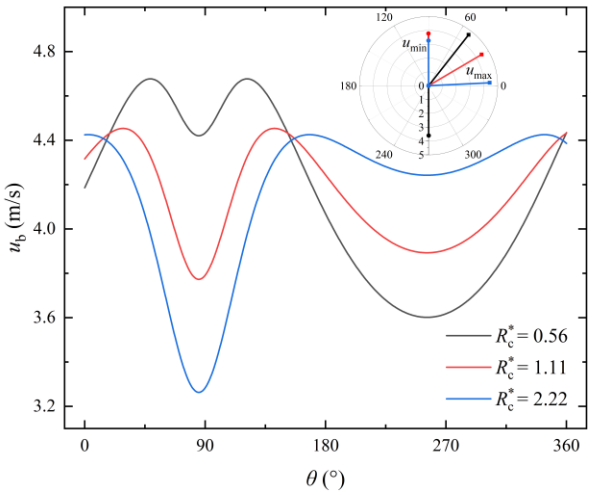


FIG. 5. The velocity distribution on the bubble interface with different cylinder radii (R_c^*) at $l^* = 2.5$.

Next, the contributions of the two boundaries to the liquid velocity in the region between the bubble and the cylinder are analyzed. Figure 6 shows the respective

contributions of the cylinder and the free surface to the liquid velocity. In the figure, the liquid velocity exhibits a rising trend with increasing distance from the cylinder (i.e., Y^* increases). When the distance to the cylinder is small ($Y^* \le 2.12$), the cylinder's contribution to the velocity is dominant. As the distance increases ($Y^* > 2.12$), the contribution from the free surface becomes dominant. The free surface dominates the liquid velocity contribution over approximately 70% of the parametric range, whereas the cylinder predominates over the remaining 30%. Furthermore, as the cylinder radius increases, the overall liquid velocity decreases.

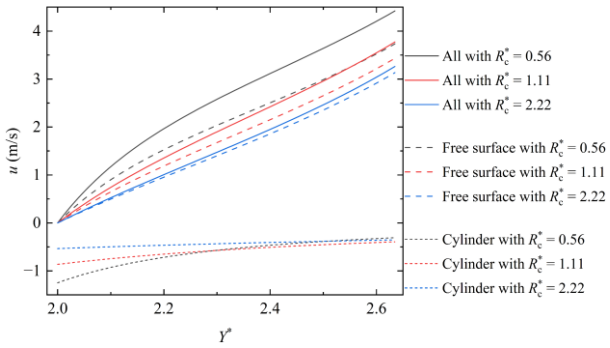


FIG. 6. Variations in the contributions of the cylinder and the free surface to the liquid velocity with Y^* at $l^* = 2.5$.

4.2 Asymmetric position

Figure 7 illustrates the velocity distribution and morphological evolution of the bubble at the asymmetric position. The red dashed arrows in the figure indicate the jet direction. As can be seen, due to the flow obstruction effect of the cylinder wall, there is a low-velocity liquid zone on the cylinder surface along the line connecting the bubble and the cylinder. In contrast, high-velocity regions are present to the right of the cylinder and in the upper-right area relative to the bubble. For the wall with a semi-cylindrical protrusion, the obstruction effect between the bubble and the wall is more pronounced. Consequently, the low-velocity region extends over a broader area, and high-velocity flow is confined solely to a narrow zone on the bubble interface distal to the cylinder.[39] As the bubble position angle (θ_b) increases, the angular extent of the high-velocity region decreases. The high-velocity region on the bubble interface gradually shifts to the right, causing the jet angle to deflect towards the left.

Next, an analysis of the bubble interface's liquid velocity is presented. Figure 8 displays the variation of the liquid velocity on the bubble interface with the circumferential angle

(θ). The liquid velocity profile is characterized by a non-monotonic evolution, exhibiting an initial increase, followed by a decrease, and a subsequent increase, which features a distinct maximum and a single minimum. As the cylinder radius increases, the position of the maximum velocity gradually shifts to the right, while the position of the minimum velocity shifts downward. This is also correlated with the variation in the jet direction as shown in Figure 7. Concurrently, the maximum velocity decreases, whereas the minimum velocity increases.

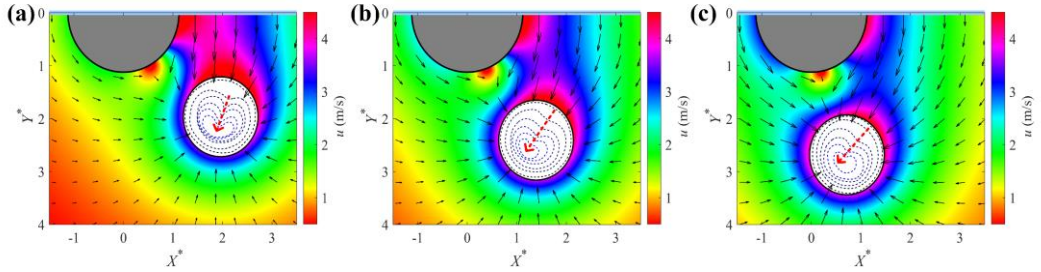


FIG.7. The liquid velocity distribution and the bubble contour evolution during the collapse with different bubble position angle (θ_b) at l^* = 2.5. (a) θ_b = 45°. (b) θ_b = 60°. (c) θ_b = 75°. The background color map and arrows denote the numerically computed velocity field, while the dashed lines indicate the experimentally observed bubble contours during collapse.

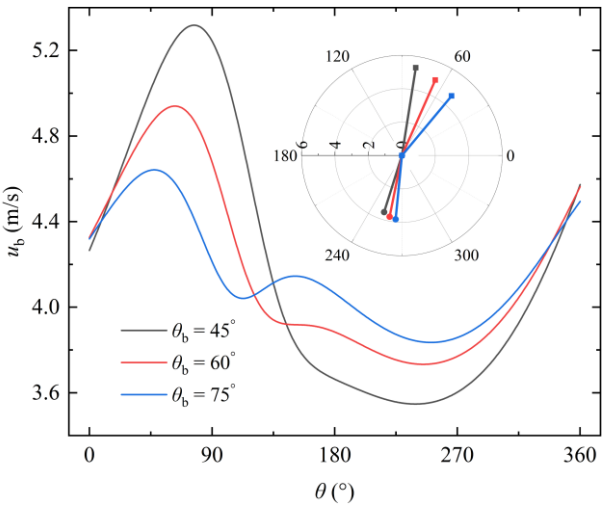


FIG. 8. The velocity distribution on the bubble interface with different bubble position angle (θ_b) at l^* = 2.5.

Subsequently, the relationship between the jet and the liquid velocity is investigated. Figure 9 shows the variation of the direction angle of the maximum liquid velocity (θ_v)

on the bubble interface and the jet direction angle (θ_j) with the dimensionless distance (l^*). Here, θ_v is obtained from theoretical calculations, and θ_j is derived from experimental mean data. All tests were conducted five times under identical conditions. Table 2 summarizes the mean values and standard deviations (SD) of θ_j for different l^*. As shown in the figure, both θ_v and θ_j exhibit a decreasing trend as l^* increases. Furthermore, as the cylinder radius increases, both θ_v and θ_j increase. The good agreement between θ_v and θ_j demonstrates that it is reasonable to use the direction of the maximum liquid velocity to predict the jet direction.

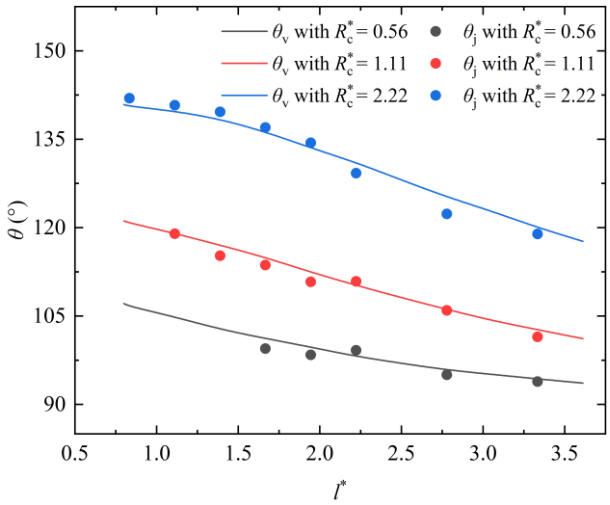


FIG. 9. Variation of the angle of the maximum liquid velocity (θ_v) on the bubble interface and the jet angle (θ_j) with the dimensionless distance (l^*) at $\theta_b = 60$.

Table 2. Mean values and standard deviations (SD) of the jet direction (θ_j) for different dimensionless distance (l^*).

R_c^* \ l^*		0.83	1.11	1.39	1.67	1.94	2.22	2.78	3.33
0.56	Mean				99.49	98.41	99.20	95.04	93.88
	SD				0.49	0.64	0.53	0.37	0.52
1.11	Mean		118.97	115.23	113.66	110.80	110.90	105.97	101.47
	SD		0.18	0.67	0.37	0.50	0.49	0.65	0.31
2.22	Mean	141.96	140.78	139.65	137.00	134.41	129.25	122.34	118.93
	SD	0.24	0.68	0.65	0.06	0.72	0.69	0.67	0.39

4.3 Jet partitioning phenomenon

Figure 10 shows the spatial distribution of the jet direction regimes. The dashed line in the figure represents the boundary between the forward jet and the counter jet. The forward jet is defined as the jet pointing towards the cylinder, while the counter jet is defined as the jet not pointing towards the cylinder. When the distance from the cylinder is small, the region of the forward jet is big. As the distance increases, the region of the forward jet shrinks. With a further increase in distance, only the counter jet exists. The forward jet exists exclusively within the regime where $l^* \leq 2.5$ and $\theta_b > 40°$.

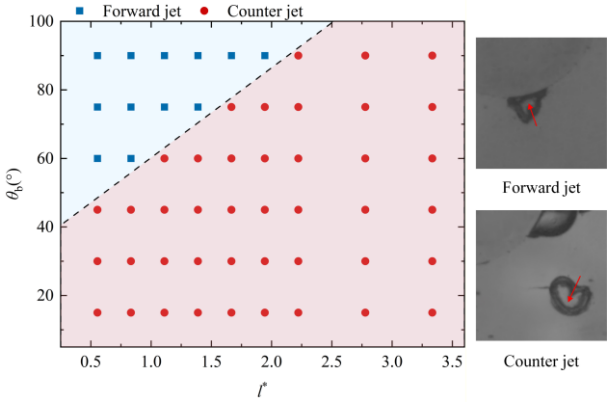


FIG. 10. The spatial distribution of the jet direction regimes.

To characterize the influence of the cylinder on the direction of the Kelvin impulse, a deviation angle ($\Delta\theta$) is defined to represent the difference between the θ_i and the θ_b:

$$\Delta\theta = |\theta_i - \theta_b|. \tag{27}$$

Figure 11 illustrates the spatial distribution of the $\Delta\theta$ and the impulse attraction region for different cylinder radii. In the subfigure (a), a larger value of the $\Delta\theta$ indicates a stronger influence of the cylinder on the impulse direction. The subfigure (b) is used to determine whether the impulse direction is oriented towards the cylinder. The attraction regions for all radii exhibit a heart-shaped distribution, and the extent of the attraction region increases as the cylinder radius increases. The spatial extent of the jet attraction zone encompasses an area approximately 1.1 times that of the cylinder.

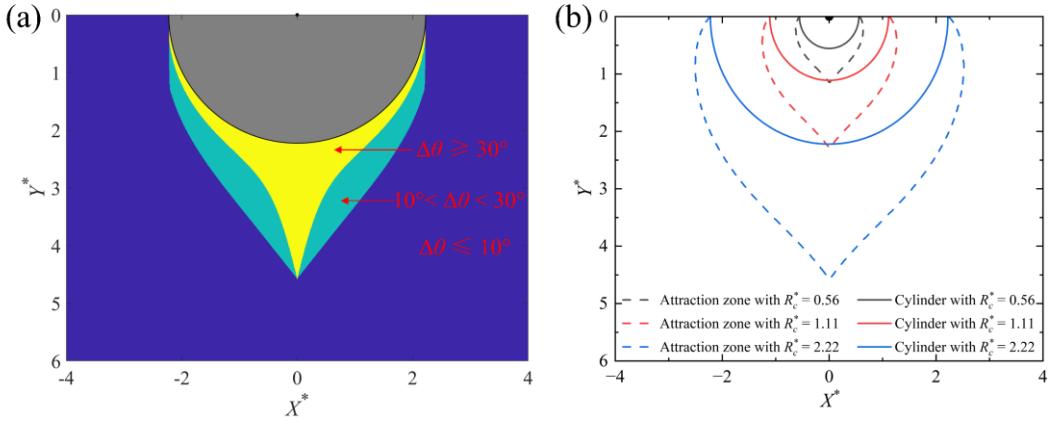


FIG. 11. The spatial distribution of the deviation angle ($\Delta\theta$) and the impulse attraction region for different cylinder radii (R_c^*). (a) The spatial distribution of the $\Delta\theta$. (b) The impulse attraction region for different cylinder radii. The yellow regions correspond to conditions where the $\Delta\theta \geq 30°$, the cyan regions represent $10° < \Delta\theta < 30°$, and the blue regions represent $\Delta\theta \leq 10°$.

5. Analysis of the bubble centroid movement

This section presents a quantitative analysis of the relationship between the bubble centroid movement and the impulse during the collapse phase. Additionally, the Kelvin impulse field and its sensitivity are analyzed, and the dominant regions of the impulse contribution from the two boundaries are defined.

Generally, the bubble's movement is attributed to the impulse acting on it. Figure 12 illustrates the variation of the impulse angle (θ_i) and the bubble centroid movement angle (θ_c) during collapse with the dimensionless distance (l^*). All tests were conducted five times under identical conditions, and θ_c represents the mean values derived from these measurements. Table 3 summarizes the mean values and SD of θ_c for different l^*. In the figure, the lines of different colors represent the theoretical values of the θ_i, while the points of different colors represent the experimental data for the θ_c during the bubble collapse phase. Here, the θ_i is defined as the angle between the impulse direction and the positive x-axis. In the figure, both θ_i and θ_c exhibit a decreasing trend as l^* increases. The rate of decrease is more significant at smaller values of l^* and becomes more gradual at larger values. As the cylinder radius increases, both θ_i and θ_c increase, but their rate of decrease with respect to l^* becomes less steep. Furthermore, there is good agreement between θ_i and θ_c.

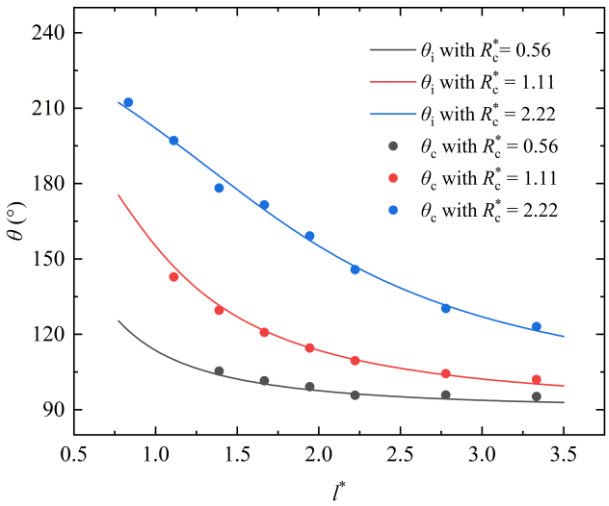


FIG. 12. Variation of the impulse angle (θ_i) and the bubble centroid movement angle (θ_c) with the dimensionless distance (l^*) at $\theta_b = 60$.

Table 3. Mean values and standard deviations (SD) of bubble centroid movement angle (θ_c) for different dimensionless distance (l^*).

R_c^* \ l^*		0.83	1.11	1.39	1.67	1.94	2.22	2.78	3.33
0.56	Mean			105.39	101.55	99.20	95.77	95.86	95.31
	SD			0.28	0.49	0.53	0.58	0.44	0.36
1.11	Mean		142.85	129.60	120.80	114.58	109.54	104.39	102.04
	SD		0.34	0.25	0.66	0.16	0.57	0.44	0.60
2.22	Mean	212.34	197.13	178.24	171.54	159.16	145.77	130.30	123.12
	SD	0.67	0.67	0.04	0.31	0.50	0.49	0.29	0.47

Subsequently, the spatial variation of the impulse within the flow field is examined. Figure 13 illustrates the distribution of the Kelvin impulse and its sensitivity. The sensitivity coefficient (ε) is defined as follows:

$$\varepsilon = \sqrt{\left(\frac{\partial \theta_i}{\partial x}\right)^2 + \left(\frac{\partial \theta_i}{\partial y}\right)^2}. \tag{28}$$

In the subfigure (a), colors represent the magnitude of the impulse, while the direction and length of the arrows denote its direction and magnitude, respectively. When the

distance to the cylinder is small, the cylinder's influence is dominant, and the impulse direction points towards the cylinder. Conversely, when the distance to the free surface is small, the free surface's influence is dominant, and the impulse direction points away from the free surface. The impulse diminishes with increasing distance from the boundaries. Directly below the cylinder, a region of minimum impulse exists due to the combined influence of the cylinder and the free surface. From subfigure (b), it is evident that the sensitivity value is higher in the vicinity of the cylinder. A region of extreme sensitivity is present directly below the cylinder. This sensitivity is attributed to the variation in the impulse direction transitions from pointing towards the cylinder to pointing away from the free surface. This region also corresponds to the area of minimum impulse observed in subfigure (a).

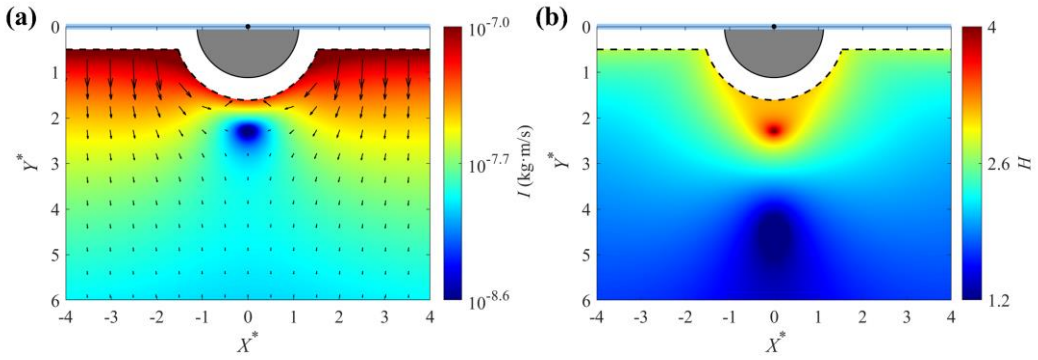


FIG. 13. The distribution of the Kelvin impulse and its sensitivity at $R_c^* = 2.22$. (a) The distribution of the Kelvin impulse. (b) The sensitivity of the Kelvin impulse.

Subsequently, the dominant roles of the two boundaries on the impulse field are analyzed to further quantify the respective contributions of the cylinder and the free surface. To facilitate this analysis, the Kelvin impulse contribution ratio (M) is defined as follows:

$$M = \frac{I_{\mathrm{fs}}}{I_{\mathrm{c}}}. \tag{29}$$

Here, I_{fs} and I_{c} respectively represent the contributions to the Kelvin impulse from the free surface and the cylinder.

Figure 14 illustrates the spatial distribution of the dominant regions associated with the

two interfaces. The red and blue dashed lines in the figure denote the regions corresponding to $M = 0.5$ and $M = 2.0$, respectively. We define the region where $M \le 0.5$ is located as the cylinder-dominated region, the region of $0.5 < M < 2.0$ as the co-dominated region, and the region of $M \ge 2.0$ as the free-surface-dominated region. As observed from the figure, the cylinder-dominated region is confined to a small area directly below the cylinder and is significantly smaller than the free-surface-dominated region. As the cylinder radius increases, the areas of both the cylinder-dominated and co-dominated regions expand, yet they remain smaller in extent than the area of the free-surface-dominated region.

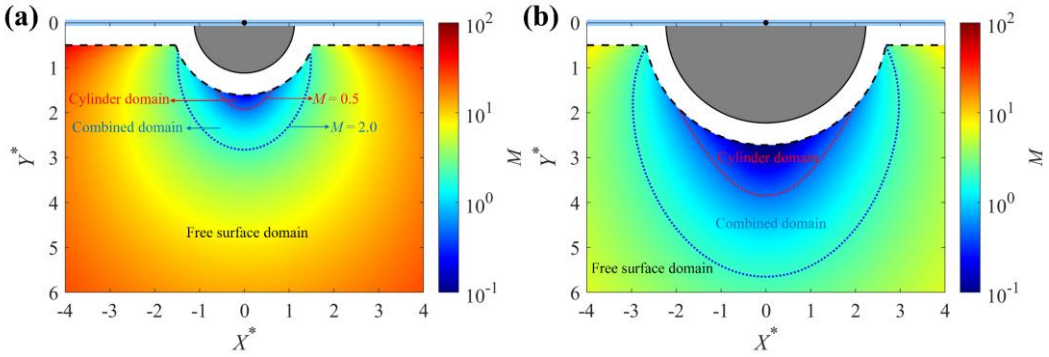


FIG. 14. The spatial distribution of the dominant regions with different cylinder radii (R_c^*). (a) R_c^* = 1.11. (b) R_c^* = 2.22.

6. Conclusions

The present paper systematically investigates the dynamic behaviors and influencing mechanisms of the bubble near the semi-submerged cylinder within confined spaces, based on the high-speed photography experiments and Kelvin impulse theory. First, a theoretical model for bubble oscillation near the semi-submerged cylinder is established. Subsequently, the liquid velocity distribution and jet characteristics during the bubble collapse process are explored. Finally, the centroid movement and Kelvin impulse during bubble collapse are elucidated both qualitatively and quantitatively. The main conclusions are outlined below:

(1) As the distance between the bubble and the cylinder (l^*) increases, the variation in jet direction is consistent with the variation in the direction of the maximum liquid velocity on the bubble interface. At $l^* = 2.5$, among the factors affecting the liquid

velocity, the free surface dominates the liquid velocity contribution over approximately 70% of the parametric range, whereas the cylinder dictates the rest.

(2) The bubble collapse jets are classified into the jet pointing towards the cylinder (forward jet) and the jet not pointing towards the cylinder (counter jet). The impulse attraction region of the cylinder is confined to a relatively small area in its vicinity, correlating with the cylinder radius and spanning approximately 1.1 times its cross-sectional area.

(3) The contributions of the cylinder and the free surface to the impulse are in opposite directions. A region of minimum impulse and a region of high sensitivity exist directly below the cylinder. The space surrounding the cylinder can be divided into a cylinder dominated region, a free surface dominated region, and a co-dominated region. The cylinder dominated region is only present near the cylinder, and its extent is significantly smaller than that of the free surface dominated region.

The present paper provides valuable insights into the cavitation erosion mechanisms pertinent to hydraulic machinery. However, it should be noted that the current theory fails near the model boundary, where the bubbles undergo significant deformation. In future work, we aim to refine this theoretical framework and employ numerical simulations to further investigate jet-induced wall erosion.

Data availability statement

The data that support the findings of this study are available from the corresponding author upon reasonable request.

Acknowledgment

This work was financially supported by the National Natural Science Foundation of China (Project Nos.: 52506045), and the Fundamental Research Funds for the Central Universities (2025JC011).

References

[1] Huang C, Li F, Feng S, Wang C, Chen S, Hu J, He R and Song J 2024 *Chin. Phys. B* **33** 024301

[2] Yu J, Liu Z, Luo J, Zhang X, Li Z and Zhang Y 2024 *J Hydrodyn* **36** 1095–103

[3] Xu L, Yao X, and Shen Y 2024 *Chin. Phys. B* **33** 044702

[4] Sarraf S S, Talabazar F R, Namli I, Maleki M, Aghdam A S, Gharib G, Grishenkov

D, Ghorbani M and Koşar A 2022 *Lab Chip* **22** 2237–58

[5] Zhang H, Fan C, Wang L, Lu W and Li D 2024 *Energies* **17** 5902

[6] Trinh Q T, Golio N, Cheng Y, Cha H, Tai K U, Ouyang L, Zhao J, Tran T S, Nguyen T-K, Zhang J, An H, Wei Z, Jerome F, Amaniampong P N and Nguyen N-T 2025 *Green Chem.* **27** 4926–58

[7] Fan M, Xu L, Hong Z, Han C and Sun Z 2026 *Renew. Energy* **256** 124400

[8] Wang J, Sun Y, Xu S and Li S 2026 *Ocean Eng* **351** 124449

[9] Yu H, Zhang X, Liu Y, Sun Y, Zhang Y, Yin Z and Li X 2024 *Constr. Build. Mater.* **447** 138182

[10] Zhao J J, Meng L H, Zhang H T, Yu M, Lin Z and Zhang G 2025 *Phys. Fluids* **37** 111301

[11] Liu N N, Wu W B, Zhang A M and Liu Y L 2017 *Phys. Fluids* **29** 107102

[12] Koukouvinis P, Gavaises M, Supponen O and Farhat M 2016 *Phys. Fluids* **28** 052103

[13] Li T, Zhang A M, Wang S P, Li S and Liu W T 2019 *Phys. Fluids* **31** 042104

[14] Zwaan E, Le Gac S, Tsuji K and Ohl C-D 2007 *Phys. Rev. Lett.* **98** 254501

[15] Wang N, Xu H, Wang T and Che Z 2024 *Phys. Fluids* **36** 042101

[16] Zi D, He D, Yao Z, Wang F, Zhong Q and Lyu P 2023 *J Hydrodyn* **35** 1064–76

[17] Liu X J, Liu W T, Ming F R, Liu Y L and Zhang A M 2024 *J. Fluid Mech* **988** A53

[18] Zhang A M, Cui P and Wang Y 2013 *Exp Fluids* **54** 1602

[19] Plesset M S and Chapman R B 1971 *J. Fluid Mech* **47** 283–90

[20] Lauterborn W and Bolle H 1975 *J. Fluid Mech* **72** 391–9

[21] Brujan E A, Keen G S, Vogel A and Blake J R 2002 *Phys. Fluids* **14** 85–92

[22] Tomita Y, Robinson P B, Tong R P and Blake J R 2002 *J. Fluid Mech* **466** 259–83

[23] Bhola S, Jr M R, Beig S A, Barbier C N and Johnsen E 2025 *J. Fluid Mech* **1004** A3

[24] Shen X, Han W, Li R, Yang S, Meng Q, Nan H, Bai L and Dong Y 2025 *Chem. Eng. Sci.* **318** 122165

[25] Wang X, Wu G, Shen J, Sun Z, Zhang Y, Zhang L and Zhang Y 2023 *Phys. Fluids* **35** 073335

[26] Shen J, Tang X, Liu W, Ma S, Luo P, Zhang Y and Zhang Y 2025 *Phys. Fluids* **37** 013307

[27] Boulton-Stone J M and Blake J R 1993 *J. Fluid Mech* **254** 437–66

[28] Zhang T, Zhang A M, Zhang S, Long S, Han R, Liu L, Ohl C-D and Li S 2025 *J. Fluid Mech* **1003** A4

[29] Ma S, Shen J, Xiong J, Zhong D, Luo P, Zhang Y and Zhang Y 2025 *Phys. Fluids* **37** 083373

[30] Han R, Zhang A M, Tan S and Li S 2022 *J. Fluid Mech* **932** A8

[31] Li S, Zhao Z, Zhang A M and Han R 2024 *J. Fluid Mech* **979** A47

[32] Kiyama A, Shimazaki T, Gordillo J M and Tagawa Y 2021 *Phys. Rev. Fluids* **6** 083601

[33] Sun Y, Fan Y, Yao Z, Wang F and Ohl C-D 2025 *Ultrason. Sonochem.* **121** 107560

[34] Noon A A and Kim M H 2021 *Energies* **14(6)** 1516.

[35] Xin Q, Cheng T, Hong J, Wang C, Liu F and Xiao Y 2025 *Flow Meas. Instrum*. **104** 102896.

[36] Best J P and Blake J R 1994 *J. Fluid Mech* **261** 75–93

[37] Ilinskii Y A, Zabolotskaya E A, Hay T A and Hamilton M F 2012 *J. Acoust. Soc. Am.* **132** 1346–57

[38] Shen J, Liu W, Zhang T, Xu Q, Luo P, Zhang Y and Zhang Y 2025 *Phys. Fluids* **37** 073358

[39] Wang X, Wu G, Zheng X, Du X, Zhang Y and Zhang Y 2025 *Ultrason. Sonochem.* **89** 106130